HHS Public Access

Author manuscript

Nano Res. Author manuscript; available in PMC 2020 December 11.

Published in final edited form as:

Nano Res. 2019 ; 12: 1381–1388. doi:10.1007/s12274-019-2340-9.

A novel near-infrared light responsive 4D printed nanoarchitecture with dynamically and remotely controllable transformation

Haitao Cui[1,§], **Shida Miao**[1,§], **Timothy Esworthy**[1], **Se-jun Lee**[1], **Xuan Zhou**[1], **Sung Yun Hann**[1], **Thomas J. Webster**[2], **Brent T. Harris**[3], **Lijie Grace Zhang**[1,4,5,6]

[1]Department of Mechanical and Aerospace Engineering, The George Washington University, Washington, DC 20052, USA

[2]Department of Chemical Engineering, Northeastern University, Boston, MA 02115, USA

[3]Department of Neurology and Pathology, Georgetown University, Washington, DC 20007, USA

[4]Departments of Electrical and Computer Engineering, The George Washington University, Washington, DC 20052, USA

[5]Department of Biomedical Engineering, The George Washington University, Washington, DC 20052, USA

[6]Department of Medicine, The George Washington University, Washington, DC 20052, USA

Abstract

Four-dimensional (4D) printing is an emerging and highly innovative additive manufacturing process by which to fabricate pre-designed, self-assembly structures with the ability to transform over time. However, one of the critical challenges of 4D printing is the lack of advanced 4D printing systems that not only meet all the essential requirements of shape change but also possess smart, dynamic capabilities to spatiotemporally and instantly control the shape-transformation process. Here, we present a facile 4D printing platform which incorporates nanomaterials into the conventional stimuli-responsive polymer, allowing the 4D printed object to achieve a dynamic and remote controlled, on-time and position shape transformation. A proof-of-concept 4D printed brain model was created using near-infrared light (NIR) responsive nanocomposite to evaluate the capacity for controllable 4D transformation, and the feasibility of photothermal stimulation for modulating neural stem cell behaviors. This novel 4D printing strategy can not only be used to create dynamic 3D patterned biological structures that can spatiotemporally control their shapes or behaviors of transformation under a human benign stimulus (NIR), but can also provide a potential method for building complex self-morphing objects for widespread applications.

Address correspondence to lgzhang@gwu.edu.

[§]Haitao Cui and Shida Miao contributed equally to this work.

Electronic Supplementary Material: Supplementary material (tensile data, and movie of NIR sensitive 4D models) is available in the online version of this article at https://doi.org/10.1007/s12274-019-2340-9.

Keywords

near-infrared light responsive; 4D printing; dynamically and remotely controllable; graphene; brain; neural stem cell

1 Introduction

Four-dimensional (4D) printing is emerging as a next-generation additive manufacturing technology, which incorporates shape transformation within the material/structural design, allowing a printed object to be reprogrammed in form or function to perform a mechanical reassembly under external stimuli [1]. This printing technique has attracted substantial attention in various research fields, such as smart optic/electronic devices, micro/nano-actuators, intelligent manufacturing, and biomedical researches [2]. Beyond creating a complex, biomimetic architecture using three-dimensional (3D) printing methodologies [3–6], 4D printing offers great potential for fabricating dynamic biological structures for biomedical applications [7, 8]. Such 4D processes may elicit proper biological responses that not only mimic the dynamic growth regimes of native tissues/organs but also achieve a more complex, dynamic architecture for tissue implants that meet the criteria of multiple shape variations with precisely controlled stimuli processes [1, 3, 9].

The characteristics of 4D shape transformation or reprogramming are classified by different mechanisms [1, 2, 10]. One of the typical mechanisms is the anisotropic structural or material design of the printed objects [1, 9]. It has been achieved through aligned/orientated printing, deposition of heterogeneous ink materials with differential properties, and varying the crosslinking/deposition density of inks [11–13]. Another typical mechanism is a change in the intrinsic physiochemical properties of printed materials. Several stimuli-responsive materials have been utilized in 4D printing, including shape memory materials and self-healing materials [1, 14–17]. Typically, 4D printed shape memory polymers (SMPs) undergo a reprogramming process based on either phase segregation of thermoplastics or thermal transition of thermosets when exposed to temperature, chemicals, or other stimuli [11, 17–20]. Although some pioneering examples demonstrated the potential to achieve shape transformation of printed objects, the current 4D printing techniques have yet to achieve remote, precise control of on-time and position of transformation.

In general, a lack of advanced printable and stimuli-responsive smart system limits the development of 4D printing techniques [1, 9]. Nanomaterials have many interesting physical and chemical properties that have been used in biomedical applications [21–24]. For example, as typical carbon-based nanomaterials, graphene and its analogs possess outstanding properties such as a high surface to volume ratio, a high aspect ratio, an excellent photothermal property, a low electrical resistivity, a high thermal conductivity, and a high modulus as well as excellent biocompatibility [22, 25, 26]. Although they have been used to create 3D printed scaffolds with good electroconductivity or strong adsorption capacity for bone, neural, and cartilage tissue engineering [27, 28], in-depth studies are required to explore their further biological potentials. It is expected, by incorporating the unique physiochemical characteristics of nanomaterials into any printable material, the novel

nanocomposites can exhibit a plethora of outstanding advantages, which provide a potential method to solve the current challenge.

In this study, we developed a novel near-infrared light (NIR) responsive 4D printed nanocomposite, which incorporates photothermal graphene into thermally responsive SMP. Graphene can absorb photons of NIR illumination to produce thermal energy. Above the glass transition temperature (T_g) of SMP, the printed object transforms its shape via a "thermomechanical reprogramming" process. Compared to directly thermally-triggered shape changing processes, light-switch stimulation can achieve a remote, precise, and dynamic control on both time and position. More importantly, long-wavelength NIR is regarded as a human benign energy form capable of efficiently penetrating tissue with no biological harm when compared to other energy sources. To the best of our knowledge, this is the first study proposing remotely and dynamically controllable 4D printing technique, and culminating a proof of concept 4D printed brain model.

2 Results and discussion

The chemical structures of the nanocomposite including thermally responsive SMP and photothermally responsive graphene are shown in Fig. 1(a). The SMP consists of a rigid epoxy monomer (bisphenol A diglycidyl ether, BDE), an aliphatic diamine crosslinker (poly(propylene glycol) bis(2-aminopropyl) ether, PBE), and a crosslinking modulator (decylamine, DA, which is used to tailor the T_g of the polymers). The different formulations were optimized to obtain the targeted SMP with transformation temperature (T_{tran}) around 45 °C [29]. Its Ttran was slightly higher than 37 °C, ensuring an effective shape fixation at cell culture temperature. The optimal molar ratio of the composition is 0.01 mol BDE, 0.003 mol PBE, and 0.004 mol DA. Graphene nanoplatelets (6–8 nm thick × 5 μm wide) at different concentrations were dispersed into the epoxy ink system without the use of any solvent. The effect of mechanical stirring, sonication time, storage time, and graphene concentration on the dispersion and reaggregation of graphene in epoxy mixtures was also analyzed according to a previous study [30]. Due to the strong van der Waals force (high viscosity) of ink and the **π-π** stacking between rigid aromatic epoxy and dispersed graphene, graphene was homogeneously dispersed in the ink without a pronounced tendency of reaggregation. To study the printability of our nanocomposite inks in the extrusion system, the dynamic viscosity was measured by rheometer at room temperature. Figure 1(b) shows the nanocomposite inks had a typical shear thinning behavior, and the viscosity of the inks increased with increasing graphene content. We found that it was hard to extrude the ink in our printing system when the graphene concentration was higher than 20%. Therefore, the nanocomposite inks with 0%, 4%, 8%, 12%, 16% and 20% graphene were systematically investigated. In a reported study, 3D printed high-content graphene scaffolds have been developed, indicating the high content graphene (> 60%) possessed good biocompatibility, which was verified by *in vitro* and *in vivo* studies [27].

The Raman spectra of samples were characterized as shown in Fig. 1(c). The D-mode appeared at approximately 1,350 cm^{-1}, the G-mode was located around 1,580 cm^{-1}, and the 2D-mode peak was at approximately 2,710 cm^{-1}, which are the three prominent peaks of graphene nanoplatelets. With increasing graphene content, some new peaks appeared around

820, 1,100, 2,850, and 2,950 cm^{-1}, which indicated the intermolecular interactions of the aromatic epoxy/graphene and graphene/graphene in epoxy. Differential scanning calorimetry (DSC) analysis (Fig. 1(d)) indicated that these samples had T_g of ~ 45 °C (that is also T_{tran} of 4D changing), and there was not any significant change observed when varying the graphene content. No melting peak was noticed, indicating the SMPs were highly cross-linked and had no crystalline domains. In the glass phase (lower than T_g), the material is rigid and cannot be easily bent; while the temperature increases beyond T_g the material enters the soft rubber phase and its malleability increases. The reversible transition between these two phases of SMPs (glass and rubber) results in the sequential shape memory cycle.

To study the thermosensitive shape memory effect, the printed nanocomposite samples were bent into a U shape at 60 °C, and the temporary shape was kept at room temperature. When the samples were placed in a thermostat (external temperature or triggering temperature is above T_g), they recovered their initial and permanent shape over time. The strain recovery rate *(R_r)* is the ability of the material to recover to its permanent shape, and the ability of the switching Segments to hold the applied mechanical deformation is called the strain fixity rate (R_f). After the calculation, our samples exhibited an R_f of ~ 99%, and an R_r of ~ 95%, suggesting the samples almost returned to their full original shape (calculation formulas of R_f and R_r are shown in Methods 4.4). The addition of graphene did not affect the original shape memory behaviors of the SMP (an R_f of ~ 99%, and an R_r of ~ 95%). Additionally, the shape-changing (transformation) duration was distinctly different by varying the triggering temperature. As shown in Fig. 2(a), the transformation time considerably decreased with increasing triggering temperature. The mechanical behavior of the nanocomposites was characterized at room temperature via uniaxial tensile testing, and the results are shown in Figs. 2(b) and 2(c). Details of tensile curves were also shown in Fig. S1 in the Electronic Supplementary Material (ESM). Compared to pure material (0%), the nanocomposites had a lower modulus, indicating the doping of graphene negatively affected the intrinsic structure of the pure epoxy. The tensile modulus of the nanocomposites increased with increasing graphene content, indicating the reinforcement effects of the graphene in the epoxy. Additionally, the nanocomposite doped with 16% graphene showed a similar tensile modulus value with the pure material. However, the extension value of nanocomposite was significantly lower. This suggests that the doping of graphene increased the material's rigidity while depreciating its malleability. Furthermore, the microstructure characteristics of the epoxy and its nanocomposites were studied using SEM as shown in Fig. 2(d). The cross-sectional images exhibited that pure epoxy had a smooth, fractured surface while graphene doping led to lamellar microstructures. Therefore, it is deduced that the different microstructures contributed to the large difference between mechanical moduli. After the porous structure was introduced, the tensile moduli decreased compared to pure material. With increasing graphene content, a denser lamellar arrangement increased the material's rigidity.

Figure 3 shows the schematic of the dynamically controllable transformation of our 4D printed NIR sensitive SMPs. After printing, the nanocomposite construct has an initial shape at room temperature (I). The nanocomposite construct is exposed to NIR illumination for heating (a photothermal-triggered process) or directly heated (a conventional thermal-triggered process) to a temperature above the triggering temperature (or T_g). A stress is

applied at $T > T_g$, where construct's shape is changed by an external force (II). The temperature of the construct is decreased, and then the stress is removed. At this stage, the construct's shape is changed and fixed (III) at room temperature (Phase 1). Once reheating up to the T_g through NIR exposure, the temporary shape of the construct can gradually return to its original shape (III → IV→ V →→→ I). During this photothermal process, the NIR illumination is able to remotely control the shape-changing position and transformation time of the nanocomposite constructs (Phase 2 → Phase 3). Figure 4 and Movie ESM1 show the NIR sensitive 4D transformation behavior of the nanocomposite models, which is different from the uncontrollable shape changing in a thermal-triggered 4D changing process. Some typical models were 4D printed, including a blooming flower, hand gesture, exerciser, controllable circuit switch, folded brain, and dilated heart. After a temporary shape was fixed, the 4D printed models were heated to recover the original shape. The traditional "thermal-triggered" recovery process is not easy to control, although local heating can be applied. Comparatively, the "photothermal-triggered" transformation exhibits a precisely and conveniently controllable feature. When exposed to a NIR laser, the 4D printed models experienced a gradual, targeted shape change, where the time and position of the transformation were precisely controlled by the NIR exposure. It is observed that the architectural detail of our constructs such as the petals, fingers, were able to be remotely, locally, and precisely controlled without a complicated predesign. The image also illustrated the brightness of light gradually increased by dynamically controlling the connection of the circuit switch, which suggested its great potential for developing intelligent circuitries or robots.

To further explore the effect of the parameters of the NIR laser and the material components on the 4D transformation process, different nanocomposites, exposure distance, and laser intensity were systematically studied as shown in Fig. 5(a). The T_{tran} decreased with increasing graphene content for NIR exposure at either 800 or 1,800 mW, and the low laser intensity results in a more distinct decrease. This phenomenon is due to the faster heat dissipation for nanocomposites with a higher graphene content (higher thermal conductivity) when considering a dynamic balance between "photothermal triggered" heating process and heat dissipation. To obtain a similar photothermal temperature, a shorter exposure distance was applied for the NIR exposure with low laser intensity. This means a higher laser intensity is able to achieve the remote control of 4D transformation, which is an additional advantage for NIR responsive 4D printing. Moreover, the nanocomposites with a lower graphene content (0.5%) also exhibited an excellent photothermal effect (not shown here), but pure epoxy kept a constant temperature (room temperature) in any case.

As the graphene nanoplatelets were applied in our design, the resulting electroconductive and optoelectronic properties of the nanocomposites were also important physical characteristics. It is expected that these unique features of nanocomposites could improve cellular functions, including signal transmission of neural cells and the autonomous beating of cardiomyocytes for electroactive tissue regeneration applications [31, 32]. Figure 5(b) shows the cyclic voltammograms (CVs) that characterize the redox properties of nanocomposites. Our results showed that the 4D printed nanocomposites doped with 12%, 16%, and 20% graphene underwent reversible redox reactions, where the enclosed area of one CV cycle is proportional to the charge storage capacity [32–34]. There is no curve

observed for other samples with lower graphene content, suggesting their non-electroactivity or nonconductivity. Similar conductivity results were also confirmed by the 4-Point sheet resistance testing. The conductivities of nanocomposites with 12%, 16%, and 20% graphene were ~ 5×10^{-5}, 1.27×10^{-4}, 5.32×10^{-4} S/m, respectively, which are within the electroconductivity range of conductors. Other samples were nonconductive (lower than 1×10^{-6} S/m). Moreover, a slight and damped photocurrent was detected when the nanocomposite was exposed to NIR illumination (Fig. 5(c)). This simple trial indicated our nanocomposite could produce and deliver charge under light illumination, although its performance is unlikely to reach the qualification of other photocurrent devices. Bioelectricity plays an essential role in the functioning of all living organisms, not just in the action potentials of nerves and muscles, but also in regulating cellular functions. In the future, we expect that a perfect tissue construct with high optoelectronic conversion efficiency can be created to produce higher charge density, which is able to improve the electroactivity of engineered tissue without the need for a complicated stimulation device. Additionally, cell proliferation and morphology were evaluated, where NE-4C neural stem cells (NSCs) were seeded on the different printed samples (Figs. 5(d) and 5(e)). After 7 days of culture, there is no significant difference among pure epoxy and nanocomposites by varying the doped graphene content. All samples exhibited excellent cell spreading morphology identified by F-actin staining. This suggests that although a high graphene content was used in our nanocomposites, our materials exhibited an excellent cytocompatibility.

Considering an appropriate printability, high mechanical strength, conductivity, and cell growth, the 16% nanocomposite ink was selected to conduct the following studies. A 4D printed brain model was designed, and NSCs were utilized to create the neural tissue construct. The brain constructs incubated in culture medium exhibited an excellent “shape fixation-NIR triggered 4D recovery” process as shown in Fig. 6(a). After creating the tissue construct, the 3D construct was temporarily fixed to a flat shape. Then NSCs were seeded onto the flat surface of the construct and further cultured for several days. After experiencing the neural differentiation, the cell-laden construct was mildly exposed to NIR illumination for recovering the original 3D brain shape. The thermal image showed the exposure region of NIR laser had a high and focused temperature distribution on our 4D printed construct. Owing largely to gravity, cells immediately exhibited a non-uniform distribution and migrated to lower areas prior to adhesion. Figure 6(b) shows fluorescent images of the NSC distribution on the 4D brain construct by confocal microscopy when the temporary flat shape of construct changed to the original folded brain-like shape under NIR exposure. It indicated our 4D printed construct was able to obtain a uniform cell distribution on the complex 3D architecture after shape transformation. To further investigate the cell viability under photothermal transformation process, different photothermal temperatures were applied, and the results are shown in Figs. 6(c) and 6(d). With increasing temperature, a significant decrease in cell viability was observed. And fluorescent microscopy images showed the number of green fluorescent protein transfected NSCs (GFP-NSCs) decreased after light exposure. However, above the T_{tran} of 4D transformation, cell viability (%) was higher than 60%, ensuring sufficient cell number on the engineered tissue construct after photothermal transformation. Furthermore, the NSC differentiation study was performed

after 2 weeks of differentiation medium culture, and results were shown in Fig. 6(e). During the differentiation culture, intermittent NIR illumination was applied to our nanocomposite construct to achieve a 4D transformation associating with an optoelectronic stimulation. The immunofluorescent images illustrated obvious differentiated neurons identified by neuron-specific Class III β-tubulin (TuJ1) and microtubule-associated protein 2 (MAP2), and some astrocytes detected by glial fibrillary acidic protein (GFAP). TuJ1 was expressed in newly generated immature neurons; when a mature neuron was generated, involving in microtubule assembly, MAP2 was detected as an essential step in neurite formation [35]. Additionally, star-shaped glial cells in the brain known as astrocytes were also found. Compared to a pure epoxy construct, a higher expression of the neurogenic protein was observed on our nanocomposite construct. It is hypothesized the bioelectricity could improve the neurogenic differentiation during the culture period. In general, our 4D printed nanocomposite construct exhibited a high potential in neural engineering. When taking *in vivo* implantation into consideration, the lowest possible graphene and the use of biodegradable polymer are required for future studies. More importantly, our current study successfully created an *in vitro* 4D printed organ model to achieve a novel concept about NIR responsive 4D printing, further illustrating the advantages of our 4D transformation system, i.e., ease of operation, high biosafety, NIR sensitivity, remote and dynamic control as well as spatiotemporal synergy. It is highly expected that this novel 4D printing technique also has great potential for other applications, such as intelligent robots and controllable circuits.

3 Conclusions

A smart epoxy with a shape memory property was synthesized, and its graphene doped nanocomposites exhibited an excellent photothermal effect. Compared to other 4D printed materials, our NIR responsive 4D printed nanocomposite possessed a dynamically and remotely controllable transformation in a spatiotemporal manner. A proof-of-concept 4D printed brain construct was developed in this study, which provides a facile method for fabricating a dynamic tissue construct to satisfy demands on structures and functions. By combining with its electroconductive and optoelectronic properties, the 4D neural cell-laden construct exhibited excellent neural stem cell growth and differentiation. This study demonstrated that the novel NIR responsive 4D printing with remotely spatiotemporal control and nanomaterials could serve as a promising strategy for future biomedical and other various applications.

4 Methods

4.1 Preparation of 4D printing ink and printability

Bisphenol A diglycidyl ether, decylamine and poly(propylene glycol) bis(2-aminopropyl) ether were purchased from Sigma. By varying the formulations of these components, the different epoxy polymers were synthesized. Three monomer chemicals were melted and mixed in an oven at 50 °C for 5 min. After thermally curing at 70 °C for 48 h, the shape memory properties of epoxy samples were investigated to obtain an optimal formulation. Graphene nanoplatelets (6–8 nm thick × 5 μm wide) were obtained from Strem Chemicals Inc. The graphene nanoplatelets with different concentrations were weighed and added in

the monomer mixture. The nanocomposite inks were melted at 50 °C for 5 min, uniformly dispersed by mechanically stirring for 5min, and then sonicated for 10 min. The viscosity of the inks was analyzed with an MCR 302 rheometer (Anton Paar), and the inks were placed on cone plates of 25 mm diameter and a gap of 104 μm.

4.2 Architecture design and printing

A dual printing technique was developed in our experiment, which consists of fused deposition modeling and extrusion printing. The 3D architectures were designed with the software Autodesk123D (Autodesk Inc.) and saved as .stl files. After the .stl files were uploaded, the 3D pre-molds were manufactured by fused deposition modeling printer with polyvinyl alcohol (PVA) filament (MakerBot Industries) similar to our previous papers [36, 37]. The typical parameters including infill density (100%), the printing speed (25 mm/s), printing temperature (200 °C) and layer height (200 μm) were used. Other parameters assigned in Slic3r include: 150 μm first layer height; vertical shells—perimeters 0; horizontal shells—solid layers, top 0, bottom 0; 90° infill angle, 10 mm^2 solid infill threshold area; skirt, loop 0; extrusion width, the first layer 0%. The nanocomposite inks were preheated to 50 °C and extruded into 3D printed molds at room temperature using a customized extrusion printer developed in our lab. The printing parameters were set to 100% infill, the printing speed of 10 mm/s, and 0.5–1 mm in layer height. The 4D constructs were cured at room temperature for 24 h followed by post-curing at 70 °C in an oven for 24 h. After polymerization, the samples were washed overnight in ethanol to remove unpolymerized ink and then soaked in boiled water for several times to purify the samples. The Raman spectra of graphene and nanocomposites were conducted with 3,000−100 cm^{-1} wavelength range using a LabRAM HR Evolution Raman spectroscope (HORIBA Scientific).

4.3 Microstructural morphologies, thermal properties, and mechanical properties

Morphological analysis of the cured samples was performed after they were gold sputter-coating via an extreme high-resolution field emission scanning electron microscopy (SEM) mode (FEI FIBSEM) under an accelerating voltage of 5 kV. The T_g of the samples was measured with a multi-cell differential scanning calorimeter (MC DSC) from TA Instruments (New Castle, DE) at a programmed ramp rate of 1 °C/min. The sample was first heated from 25 to 150 °C, and held at 150 °C for 1 min. Then the sample was cooled from 150 to −30 °C, and held at −30 °C for 1 min. A second cycle was conducted: heating from −30 to 150 °C, holding 1 min and decreasing from 150 to −30 °C. The second cycle was used to determine the T_g. Tensile testing of the samples was conducted using a uniaxial mechanical tester (MTS Criterion Model 43). The samples were mounted on the 5 kN load cell and pulled at a rate of 0.5 mm/min until failure. Data were taken using TW software and Young's modulus was determined by the linear portion of the tensile stress-strain curve.

4.4 Shape memory properties and photothermal properties

Shape memory tests were conducted according to our previously reported method [18]. The samples were printed into 50 mm × 5 mm strips, and folded 180° at 60 °C into a "U" shape with an inner radius of 10 mm, and kept at this temperature for 10 min. The samples were then immediately cooled to room temperature and maintained at this temperature for an

additional 10 min. The fixed angle of the specimen was determined and recorded as θ_{fixed}. The strips were then immersed in different preset temperature to recover the permanent shape. The final angle of the specimen was determined and recorded as θ_{final}. Shape fixity (R_f) and shape recovery (R_r) were calculated by the following equations: $R_f = \theta_{fixed} / 180 \times 100\%$, and $R_r = (\theta_{fixed} - \theta_{final}) / \theta_{fixed} \times 100\%$.

After testing the material's thermally-triggered shape change, its photothermal properties were further investigated. A customized NIR laser device composed of PSU-III-LED power (0–2,000 mW, 808 nm) and 400 μm fiber cable was utilized for studying the shape recovery process. The relationship between NIR illumination and temperature change was systemically analyzed by varying exposure time, laser energy, and distance. The dynamic shape change of different models was recorded with a PowerShot ELPH 360HS Cannon camera. The temperature data and thermal images were collected using Visual IR Thermometer (FLUKE).

4.5 Electrical and optoelectronic properties

Cyclic voltammetry (CV) and Amperometric *i–t* curves of the samples were conducted on a DY2000 Series Multi-channel Potentiostat (Digi-Ivy, Inc.) using Ag/AgCl and Pt as the reference and counter electrodes, respectively. The sample was used as the working electrode, and the scan rate was 50 mV/s. For the optoelectronic study, the NIR laser was set to 2,000 mW, and the initial potential on the working electrode was 0 V. The electrical conductivity of samples was measured using 4-Point sheet resistance meter (R-CHEK).

4.6 Cell culture and differentiation

NSCs cloned from mouse neuroectoderm (NE-4C) were purchased from American Type Culture Collection (ATCC). NSCs were cultured in Eagle's minimum essential medium (ATCC) supplemented with 5% (v/v) fetal bovine serum and 1% (v/v) L-glutamine. For neuronal differentiation studies of NSCs, cells were cultured in the aforementioned complete medium supplemented with all-trans retinoic acid (RA, 10^{-6} M) [35]. All cells were incubated in a 95% humidified atmosphere with 5% CO_2 at 37 °C.

4.7 Cell viability, proliferation, and morphology

NSCs were seeded on the constructs at a density of 5×10^4 cells/mL and continuously cultured for 1, 3, and 7 days. At the predetermined time interval, the culture medium containing 10% CCK-8 solution (Dojindo, Japan) was added and incubated for 2 h. 200 μL of medium was transferred into a 96-well plate, and the absorbance at a wavelength of 450 nm was quantified by a spectrophotometer (Thermo, USA).

Specifically, at each predetermined time, all constructs were fixed with 10% formalin for 15 min and then permeabilized with 0.2% Triton-100 for 10 min. The samples were then stained with a Texas Red-X phalloidin solution (1:100) for 30 min, followed by 4',6-diamidino-2-phenylindole (DAPI) (1:1,000) solution for another 5 min. The NSC morphology on the constructs was observed using laser confocal microscopy (Carl Zeiss LSM 710).

Additionally, GFP-NSCs (NE-GFP-4C, ATCC) were seeded on the constructs at a density of 5×10^4 cells/mL and cultured for 24 h. By varying temperature in relation to laser exposure, cell viability was measured using CCK-8 kit and observed using confocal microscopy.

4.8 Immunofluorescence staining

NSCs were seeded at a density of 3×10^4 cells/mL on each sample and incubated in the aforementioned differentiation medium for 14 days to evaluate the neuronal differentiation. The samples were fixed with 10% formalin for 15 min followed by permeabilization in 0.2% Triton100 solution for 10 min at room temperature. Then the samples were incubated with blocking solution (containing 1% bovine serum albumin (BSA), 0.1% Tween 20 and 0.3 M glycine in PBS) for 2 h. The first primary antibody of mouse anti-TuJ1 (1:1,000), rabbit anti-GFAP antibody (1:500) and rabbit anti-MAP2 antibody (1:500) were gently mixed with samples overnight at 4 °C. Next, the secondary antibodies of goat anti-mouse Alexa Fluor 594 (1:1,000) and goat anti-rabbit Alexa Fluor 488 (1:1,000) were incubated with samples in the dark for 2 h at room temperature, followed by DAPI (1:1,000) solution incubation for 5 min. The immunofluorescence images were taken using confocal microscopy.

Supplementary Material

Refer to Web version on PubMed Central for supplementary material.

Acknowledgements

We would like to thank the NSF MME program grant # 1642186, NIH Director's New Innovator Award 1DP2EB020549–01 and March of Dimes Foundation's Gene Discovery and Translational Research Grant for financial support. We thank Dr. Xinran Zhang, Assistant Director of the Institute for Soft Matter Synthesis and Metrology at Georgetown University, for DSC and rheological analysis.

References

[1]. Miao SD; Castro N; Nowicki M; Xia L; Cui HT; Zhou X; Zhu W; Lee SJ; Sarkar K; Vozzi G et al. 4D printing of polymeric materials for tissue and organ regeneration. Mater. Today 2017, 20, 577–591.

[2]. Shin DG; Kim TH; Kim DE Review of 4D printing materials and their properties. Int. J. Precis. Eng. Manuf. -Green Tech 2017, 4, 349–357.

[3]. Cui HT; Nowicki M; Fisher JP; Zhang LG 3D bioprinting for organ regeneration. Adv. Healthc. Mater 2017, 6, 1601118.

[4]. Cui HT; Miao SD; Esworthy T; Zhou X; Lee SJ; Liu CY; Yu ZX; Fisher JP; Mohiuddin M; Zhang LG 3D bioprinting for cardiovascular regeneration and pharmacology. Adv. Drug Deliv. Rev 2018, 132, 252–269. [PubMed: 30053441]

[5]. Deng CJ; Yao QQ; Feng C; Li JY; Wang LM; Cheng GF; Shi MC; Chen L; Chang J; Wu CT 3D printing of bilineage constructive biomaterials for bone and cartilage regeneration. Adv. Funct. Mater 2017, 27, 1703117.

[6]. Yang BW; Yin JH; Chen Y; Pan SS; Yao HL; Gao YS; Shi JL 2D-black-phosphorus-reinforced 3D-printed scaffolds: A stepwise countermeasure for osteosarcoma. Adv. Mater 2018, 30, 1705611.

[7]. Lalwani G; D'Agati M; Khan AM; Sitharaman B Toxicology of graphene-based nanomaterials. Adv. Drug Deliv. Rev 2016, 105, 109–144. [PubMed: 27154267]

[8]. Zhao QL; Wang J; Cui HQ; Chen HX; Wang YL; Du XM Programmed shape-morphing scaffolds enabling facile 3D endothelialization. Adv. Funct. Mater 2018, 28, 1801027.

[9]. Li YC; Zhang YS; Akpek A; Shin SR; Khademhosseini A 4D bioprinting: The next-generation technology for biofabrication enabled by stimuli-responsive materials. Biofabrication 2016, 9, 012001. [PubMed: 27910820]

[10]. Choi J; Kwon OC; Jo W; Lee HJ; Moon MW 4D printing technology: A review. 3D Print. Addit. Manuf 2015, 2, 159–167.

[11]. Miao SD; Cui HT; Nowicki M; Xia L; Zhou X; Lee SJ; Zhu W; Sarkar K; Zhang ZY; Zhang LG Stereolithographic 4D bioprinting of multiresponsive architectures for neural engineering. Adv. Biosyst 2018, 2, 1800101. [PubMed: 30906853]

[12]. Gladman AS; Matsumoto EA; Nuzzo RG; Mahadevan L; Lewis JA Biomimetic 4D printing. Nat. Mater 2016, 15, 413–418. [PubMed: 26808461]

[13]. Huang LM; Jiang RQ; Wu JJ; Song JZ; Bai H; Li BG; Zhao Q; Xie T Ultrafast digital printing toward 4D shape changing materials. Adv. Mater 2017, 29, 1605390.

[14]. Lee AY; An J; Chua CK Two-way 4D printing: A review on the reversibility of 3D-printed shape memory materials. Engineering 2017, 3, 663–674.

[15]. Ding Z; Yuan C; Peng XR; Wang TJ; Qi HJ; Dunn ML Direct 4D printing via active composite materials. Sci. Adv 2017, 3, e1602890. [PubMed: 28439560]

[16]. Li WB; Liu YJ; Leng JS Selectively actuated multi-shape memory effect of a polymer multicomposite. J. Mater. Chem. A 2015, 3, 24532–24539.

[17]. Wei HQ; Zhang QW; Yao YT; Liu LW; Liu YJ; Leng JS Direct-write fabrication of 4D active shape-changing structures based on a shape memory polymer and its nanocomposite. ACS Appl. Mater. Interfaces 2017, 9, 876–883. [PubMed: 27997104]

[18]. Miao SD; Zhu W; Castro NJ; Nowicki M; Zhou X; Cui HT; Fisher JP; Zhang LG 4D printing smart biomedical scaffolds with novel soybean oil epoxidized acrylate. Sci. Rep 2016, 6, 27226. [PubMed: 27251982]

[19]. Miao SD; Cui HT; Nowicki M; Lee SJ; Almeida J; Zhou X; Zhu W; Yao XL; Masood F; Plesniak MW et al. Photolithographic-stereolithographic-tandem fabrication of 4D smart scaffolds for improved stem cell cardiomyogenic differentiation. Biofabrication 2018, 10, 035007. [PubMed: 29651999]

[20]. Miao SD; Zhu W; Castro NJ; Leng JS; Zhang LG Four-dimensional printing hierarchy scaffolds with highly biocompatible smart polymers for tissue engineering applications. Tissue Eng. Part C Methods 2016, 22, 952–963. [PubMed: 28195832]

[21]. Chen AC; Chatterjee S Nanomaterials based electrochemical sensors for biomedical applications. Chem. Soc. Rev 2013, 42, 5425–5438. [PubMed: 23508125]

[22]. Chung C; Kim YK; Shin D; Ryoo SR; Hong BH; Min DH Biomedical applications of graphene and graphene oxide. Acc. Chem. Res 2013, 46, 2211–2224. [PubMed: 23480658]

[23]. Gao JH; Gu HW; Xu B Multifunctional magnetic nanoparticles: Design, synthesis, and biomedical applications. Acc. Chem. Res 2009, 42, 1097–1107. [PubMed: 19476332]

[24]. Blum AP; Kammeyer JK; Rush AM; Callmann CE; Hahn ME; Gianneschi NC Stimuli-responsive nanomaterials for biomedical applications. J. Am. Chem. Soc. 2015, 137, 2140–2154. [PubMed: 25474531]

[25]. Shen H; Zhang LM; Liu M; Zhang ZJ Biomedical applications of graphene. Theranostics 2012, 2, 283–294. [PubMed: 22448195]

[26]. Yang YQ; Asiri AM; Tang ZW; Du D; Lin YH Graphene based materials for biomedical applications. Mater. Today 2013, 16, 365–373.

[27]. Jakus AE; Secor EB; Rutz AL; Jordan SW; Hersam MC; Shah RN Three-dimensional printing of high-content graphene scaffolds for electronic and biomedical applications. ACS Nano 2015, 9, 4636–4648. [PubMed: 25858670]

[28]. Zhou X; Nowicki M; Cui HT; Zhu W; Fang XQ; Miao SD; Lee SJ; Keidar M; Zhang LJG 3D bioprinted graphene oxide-incorporated matrix for promoting chondrogenic differentiation of human bone marrow mesenchymal stem cells. Carbon 2017, 116, 615–624.

[29]. Xie T; Rousseau IA Facile tailoring of thermal transition temperatures of epoxy shape memory polymers. Polymer 2009, 50, 1852–1856.

[30]. Wei JC; Atif R; Vo T; Inam F Graphene nanoplatelets in epoxy system: Dispersion, reaggregation, and mechanical properties of nanocomposites. J. Nanomater 2015, 2015, Article ID 561742.

[31]. Cui HT; Liu YD; Cheng YL; Zhang Z; Zhang PB; Chen XS; Wei Y *In vitro* study of electroactive tetraaniline-containing thermosensitive hydrogels for cardiac tissue engineering. Biomacromolecules 2014, 15, 1115–1123. [PubMed: 24597966]

[32]. Zhu W; Ye T; Lee SJ; Cui HT; Miao SD; Zhou X; Shuai DM; Zhang LG Enhanced neural stem cell functions in conductive annealed carbon nanofibrous scaffolds with electrical stimulation. Nanomedicine 2018, 14, 2485–2494. [PubMed: 28552650]

[33]. Cui HT; Wang Y; Cui LG; Zhang PB; Wang XH; Wei Y; Chen XS In vitro studies on regulation of osteogenic activities by electrical stimulus on biodegradable electroactive polyelectrolyte multilayers. Biomacromolecules 2014, 15, 3146–3157. [PubMed: 24995801]

[34]. Cui HT; Shao J; Wang Y; Zhang PB; Chen XS; Wei Y PLA-PEG-PLA and its electroactive tetraaniline copolymer as multi-interactive injectable hydrogels for tissue engineering. Biomacromolecules 2013, 14, 1904–1912. [PubMed: 23611017]

[35]. Zhou X; Cui HT; Nowicki M; Miao SD; Lee SJ; Masood F; Harris BT; Zhang LG Three-dimensional-bioprinted dopamine-based matrix for promoting neural regeneration. ACS Appl. Mater. Interfaces 2018, 10, 8993–9001. [PubMed: 29461046]

[36]. Cui HT; Zhu W; Holmes B; Zhang LG Biologically inspired smart release system based on 3D bioprinted perfused scaffold for vascularized tissue regeneration. Adv. Sci 2016, 3, 1600058.

[37]. Cui HT; Zhu W; Nowicki M; Zhou X; Khademhosseini A; Zhang LG Hierarchical fabrication of engineered vascularized bone biphasic constructs via dual 3D bioprinting: Integrating regional bioactive factors into architectural design. Adv. Healthc. Mater 2016, 5, 2174–2181. [PubMed: 27383032]

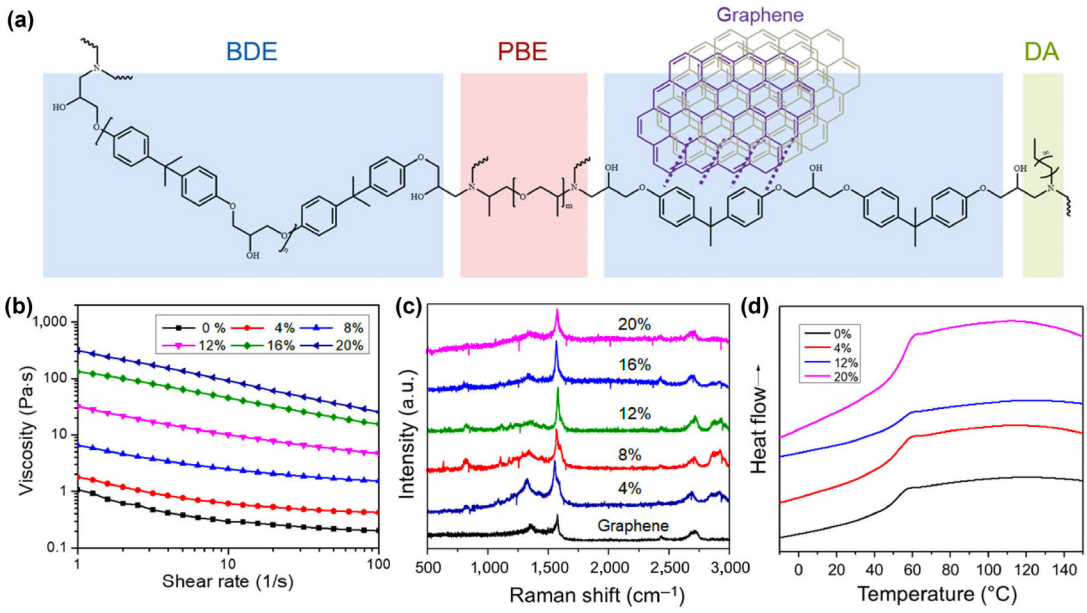

Figure 1.

Synthesis and characterization of 4D nanocomposite inks. (a) Chemical structures of the nanocomposite ink consisted of the thermally responsive SMP and photothermally responsive graphene. Dotted lines show the **π-π** interaction between SMP and graphene. The SMP includes three segments: a rigid epoxy monomer (bisphenol A diglycidyl ether, BDE), an aliphatic diamine crosslinker (poly(propylene glycol) bis(2-aminopropyl) ether, PBE), and a crosslinking modulator (decylamine, DA, which is used to tailor the *Tg* of the polymers). (b) Dynamic viscosity of 4D nanocomposité inks measured by rheometer at room temperature. It shows a typical shear thinning behavior, and the viscosity of the inks increase with increasing graphene content. (c) Raman spectra of nanocomposites and graphene. Three prominent peaks of graphene nanoplatelets are ~1,350 cm^{-1} (D-mode), ~1,580 cm^{-1} (G-mode), and ~ 2,710 cm^{-1} (2D-mode). (d) DSC curves of the nanocomposites and pure SMP. It indicates these samples have a similar T_g of 45 °C. The arrow shows the endothermic process.

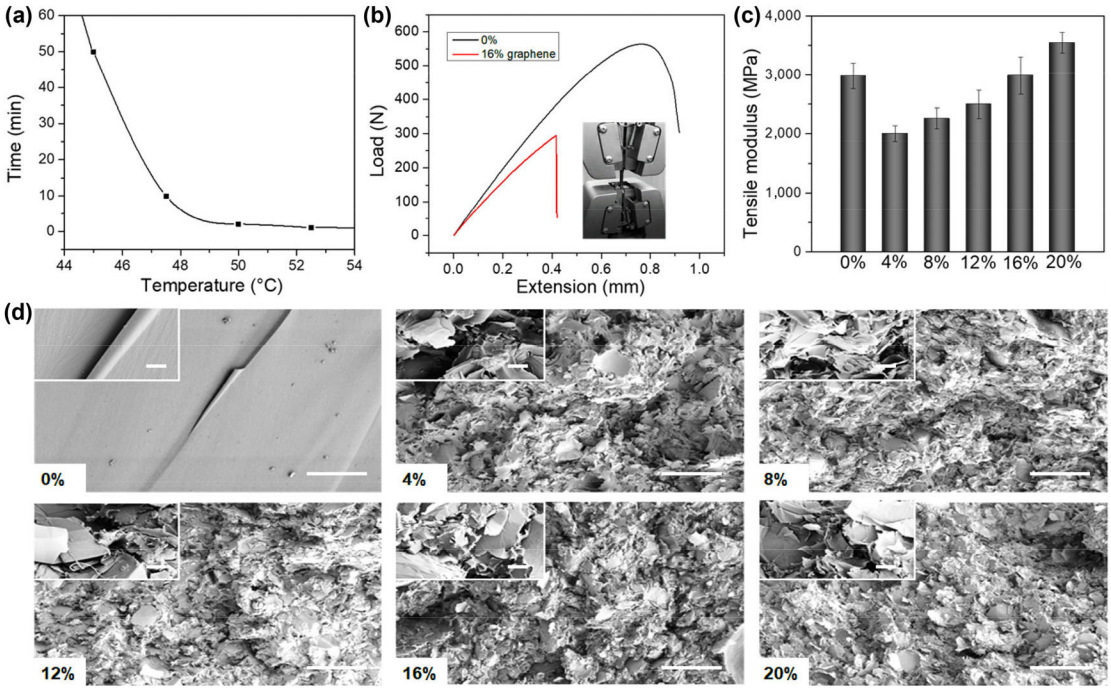

Figure 2.

Characterization of 4D printed nanocomposite constructs. (a) Shape changing (4D transformation) duration by varying the triggering temperature. (b) Load-extension curves of the nanocomposite constructs with 16% graphene and pure SMP characterized at room temperature via uniaxial tensile testing. (c) Tensile modulus of the different nanocomposite constructs. (d) Cross-sectional SEM images of different samples and the scale bar is 200 μm. The inset image shows an enlarged morphology with 10 μm scale bar.

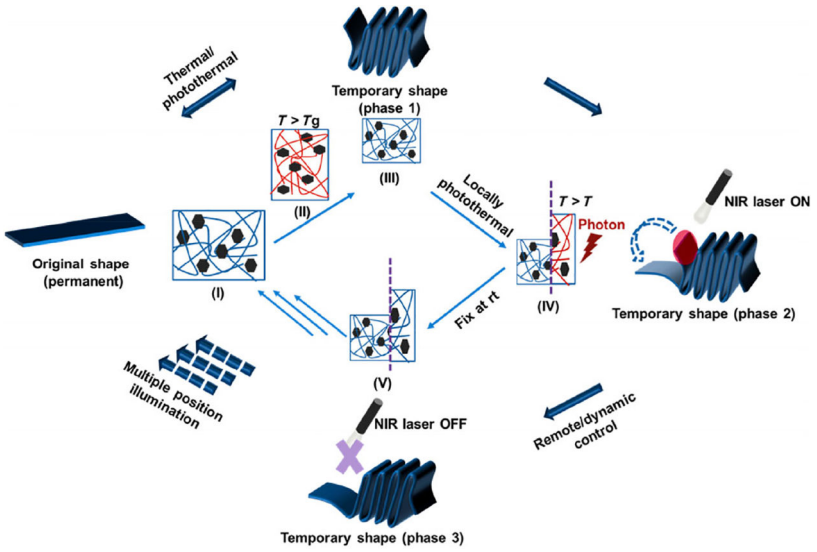

Figure 3.

Schematics of NIR sensitive 4D transformation. The printed nanocomposite construct has an initial shape (I). After exposed to NIR illumination ($T > T_g$), the construct is changed to a temporary shape by an external force (II). Then the construct's shape is fixed (III) at room temperature (Phase 1). Once heating up to the T_g through NIR exposure, the temporary shape of the construct can gradually return to its original shape (IV→V→→→I). During this photothermal process, the NIR illumination can control the shape-changing position and transformation time (Phase 2 and 3).

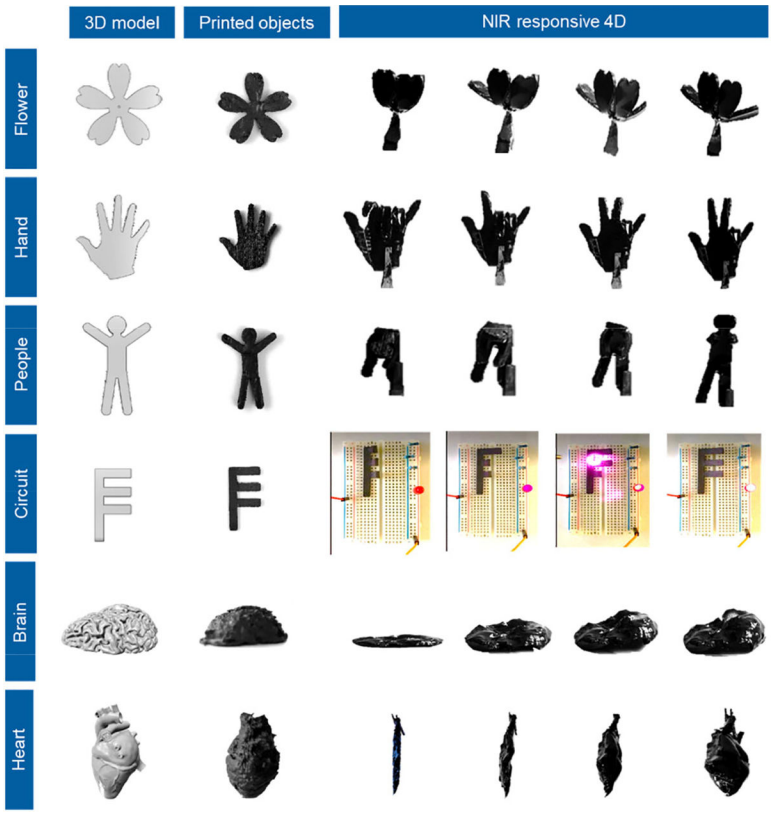

Figure 4.

Dynamically controllable transformation of 4D printed constructs. NIR sensitive 4D transformation behavior of the nanocomposite models, including a blooming flower, hand gesture, exerciser, controllable circuit switch, folded brain, and dilated heart. The shape of these models could be dynamically and precisely controlled under NIR exposure.

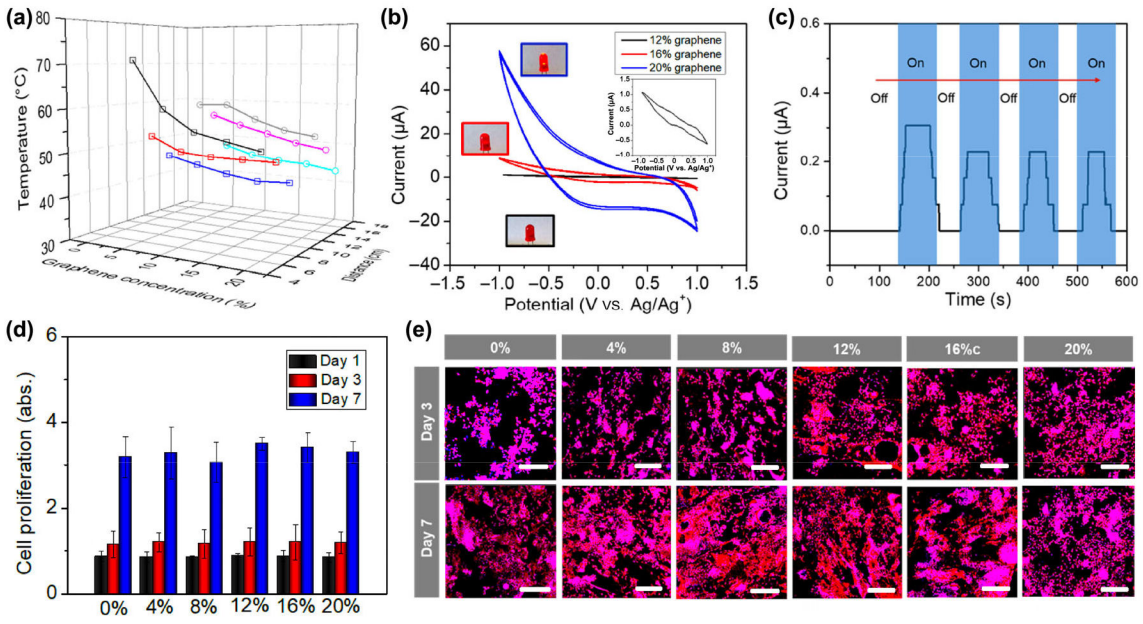

Figure 5.

Characterization of NIR sensitive 4D printed constructs. (a) Effect of the parameters of NIR laser and material component on the 4D transformation process, including different graphene content, exposure distance, and laser intension. □ represents 800 mW NIR illumination, ○ represents 1,800 mW NIR illumination; line colors show different exposure distances (− 6 cm, − 8 cm, − 10 cm, − 14 cm, − 16 cm, and − 18 cm). (b) Cyclic voltammogram curves of different nanocomposites doped with 12%, 16%, and 20% graphene. The inset curve shows nanocomposite with 12% graphene. The inset images illustrate different brightness of the lamp, where the blue frame shows 20% sample, red frame shows 16% sample, and the black frame shows 12% sample, indicating good electroconductivity of the samples. (c) Optoelectrical property of the nanocomposites with 16% graphene. When the light is on, a slight photocurrent can be detected; after the light is turned off, the photocurrent disappears. (d) NSC proliferation on different 4D printed samples after 1, 3, and 7 days of culture. (e) NSC morphology on different 4D printed samples after 3 and 7 days of culture, where F-actin is colored red and nucleus is colored blue. Scale bar is 200 μm. There is no significant difference among these samples (N.S.), suggesting graphene doped nanocomposites exhibited an excellent cytocompatibility *in vitro*.

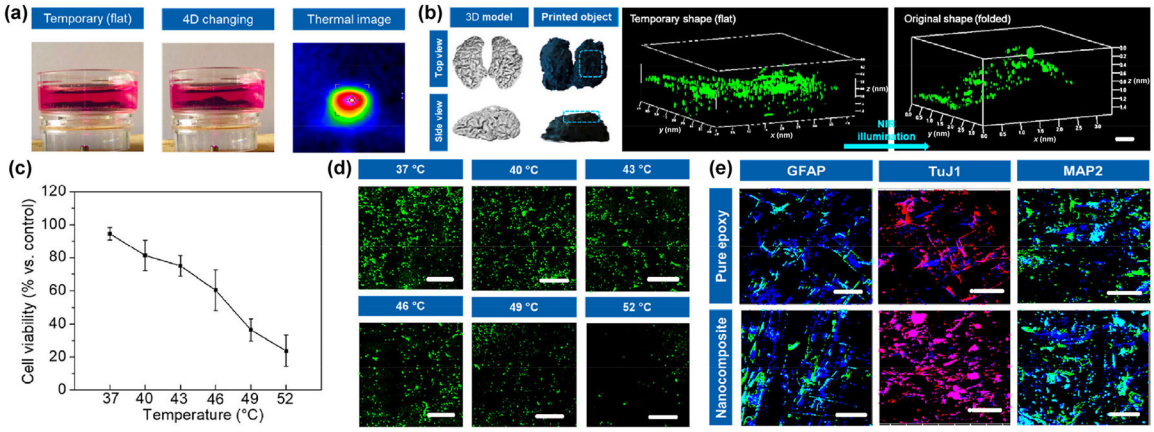

Figure 6.

NIR responsive 4D printed brain construct. (a) 4D transformation of brain constructs from a temporary flat shape to original folded shape in the culture medium, when exposed to the NIR illumination. The thermal image shows a photothermal effect. (b) GFP-NSCs distribution on 4D brain constructs when the flat shape of construct changed to folded shape. Scale bar is 500 μm. (c) NSC viability (%) measurement under different photothermal temperature when cells were exposed to NIR illumination. (d) Fluorescent images of GFP-NSCs under different photothermal temperature. Scale bar is 200 μm. (e) Immunofluorescent images of NSC differentiation on 4D printed nanocomposite brain construct compared to pure epoxy construct, after culturing in differentiation medium for 2 weeks. GFAP and MAP2 are colored green, TuJ1 is colored red, and nuclei are colored blue. Scale bar is 200 μm. During the NSC differentiation, a 4D transformation of the printed brain construct was performed under NIR exposure.